

## Revealing microstructural inhomogeneities with dark-field neutron imaging

A. Hilger,<sup>1</sup> N. Kardjilov,<sup>1</sup> T. Kandemir,<sup>1</sup> I. Manke,<sup>1</sup> J. Banhart,<sup>1</sup> D. Penumadu,<sup>2</sup>  
A. Manescu,<sup>3</sup> and M. Strobl<sup>4,a)</sup>

<sup>1</sup>Helmholtz Zentrum Berlin, Glienickerstr. 100, 14109 Berlin, Germany

<sup>2</sup>University of Tennessee, 223 Perkins Hall, Knoxville, Tennessee 37996, USA

<sup>3</sup>Università Politecnica delle Marche, Via Brecce Bianche 1, 60131 Ancona, Italy

<sup>4</sup>Ruprecht Karls University of Heidelberg, Im Neuenheimer Feld 253, 69120 Heidelberg, Germany and  
Helmholtz Zentrum Berlin, Glienickerstr. 100, 14109 Berlin, Germany

(Received 31 October 2009; accepted 29 December 2009; published online 1 February 2010)

Dark-field neutron tomography was applied to obtain three-dimensional volumetric data representing the distribution of micrometer and submicrometer sized structures in bulk samples. This is a size range that complements the range of direct spatial resolution. A phase grating setup implemented in a conventional imaging instrument enables corresponding tomographic investigations on reasonable time scales. Different samples were investigated and demonstrate the applicability of the method for the investigation of structural materials. Local variations in the small-angle scattering in BiSn, AlSi, and aluminum samples were mapped and the results are discussed with respect to the contrast formation of the method. © 2010 American Institute of Physics. [doi:10.1063/1.3298440]

Neutron imaging has seen an outstanding technical and methodical development since digital imaging detectors have become available about a decade ago.<sup>1</sup> As a consequence, state-of-the-art imaging facilities are available at many major neutron sources that provide spatial resolutions of the order of some 10  $\mu\text{m}$  (Refs. 2–4) and time resolution down to a few milliseconds.<sup>5–7</sup> Additionally, neutron imaging has become sensitive to magnetic fields and structures,<sup>8,9</sup> to crystallographic structure,<sup>10–12</sup> and to the phase of the probing radiation.<sup>13–16</sup> Neutron dark-field contrast imaging, on the other hand, interrogates the microstructure of samples through the spatially resolved detection of deviations in the (ultra-) small-angle scattering regime.<sup>17,18</sup> Thereby radiographic, but also volumetric, data visualization of the distribution and inhomogeneities of micrometer and submicrometer sized structures in bulk samples can be obtained. In contrast to the crystal analyzer based method, a grating interferometer setup<sup>16,17</sup> enables corresponding three-dimensional tomographic investigations with neutrons on reasonable time scales. While earlier reports deal with proof-of-principle experiments,<sup>18,19</sup> here, neutron dark-field contrast imaging has been applied to various samples relevant to material science in the work presented here.

Dark-field contrast is achieved due to small-angle scattering from the microstructure of a specific sample in the ultrasmall-angle regime. To detect dark-field contrast, a high angular resolution of the used setup is required. Initially neutron dark-field contrast imaging could be realized with double crystal diffractometer setups,<sup>17</sup> which are normally applied for ultrasmall-angle neutron scattering (USANS) investigations complementing the resolvable range of conventional pinhole SANS instruments in a size range between approximately 0.1 and some 10  $\mu\text{m}$ . However, a grating interferometer provides similar angular resolution but a signifi-

cantly higher efficiency for imaging due to relaxed spatial and temporal coherence requirements.<sup>16</sup> The interferometer for neutron imaging consists of three gratings. The first grating G0 is an absorption slit grating positioned behind the aperture D, which defines together with the distance to the sample L and the sample to detector distance l the geometrically achievable resolution of the imaging instrument  $d = l^*(L/D)^{-1}$ . The source grating G0, however, provides a number of partially coherent beams, which form an interference pattern behind the phase grating G1 due to periodical phase shifts in  $\pi$ . The geometry is such that the interference patterns of the beams add constructively at the first partial Talbot distance. There an absorption analyzer grating with a period corresponding to the interference pattern, which cannot be resolved by the imaging detector with an intrinsic resolution of in the best case<sup>2–4</sup> some 10  $\mu\text{m}$ , is installed. The pattern is resolved in each imaging pixel by a stepwise scan of the analyzer grating. This way, the angular and spatial resolution are decoupled and refraction as well as scattering angles of the order of some 10  $\mu\text{rad}$  (i.e., of several arcseconds) can be detected. For USANS with cold neutrons, such angles correspond to structure sizes in the micrometer range, which are beyond the spatial resolution of real space neutron imaging.

Differential phase contrast, which basically corresponds to refraction, can normally be distinguished from the small-angle scattering signal, i.e., dark-field contrast, because refraction in a certain region of a sample causes beam deviations to distinguished directions, while small-angle scattering is responsible for a symmetric broadening of the angular beam distribution. Consequently, refraction shifts the interference pattern corresponding to a certain angle while the ultrasmall-angle scattering contribution reduces the contrast of the pattern.<sup>18</sup> However, measurements show that due to the limited spatial resolution, refraction, i.e., differential phase contrast, also always affects the dark-field image. In

<sup>a)</sup>Electronic mail: strobl@helmholtz-berlin.de.

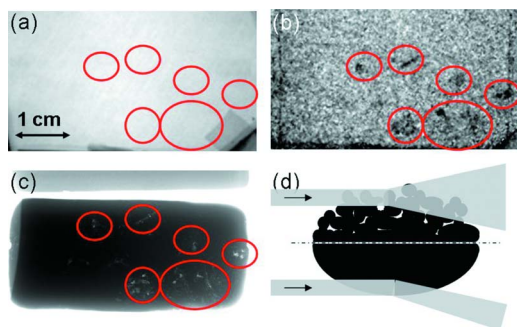


FIG. 1. (Color online) (a) Attenuation contrast radiography of BiSn plate; [(b) and (c)] dark-field contrast and an x-ray image of the sample, respectively. Circles mark main areas where inner structures are found in (b) and (c). (d) Schematic drawing of development of dark-field contrast (top) vs differential phase contrast (bottom).

certain pixels of the imaging detector, different refracted and nonrefracted contributions overlap, and hence diminish the visibility of the interference fringes.<sup>19</sup> In some of these cases, this effect hinders clear clarification of the origin of the signal and consequently an estimation of the size of structural inhomogeneities detected in the sample. In the following, the results of some applied measurements will underline these findings.

Measurements were performed using the cold neutron radiography and tomography beamline CONRAD (Ref. 20) at the BER2 research reactor of the Helmholtz Centre Berlin (former Hahn-Meitner Institute). The beam was monochromatized by the means of a double crystal device.<sup>12</sup> With typical object to detector distances of 3.5 cm, a spatial resolution better than 200  $\mu\text{m}$  could be achieved. The gratings G0, G1, and G2 had periods of 791.5, 7.96, and 4  $\mu\text{m}$ , respectively. Scans over one period of the interference pattern of the grating interferometer were performed with 20 (radiograms), respectively, 10 (tomographic projections) equidistant steps with an exposure time of 120–180 s for every step.

Three kinds of samples were investigated. The first type of samples were crystalline BiSn sheets with thicknesses of 1.4 and 0.8 mm and sizes of  $45 \times 20 \text{ mm}^2$ . These were measured radiographically. The thin and weakly attenuating samples neither provided sufficient conventional attenuation contrast [Fig. 1(a)] nor significant differential phase contrast. In contrast, the dark-field image displays several features in one of the sheets [Fig. 1(b)]. In order to learn more about the obvious structural inhomogeneities, the samples have been exposed in an x-ray imaging setup ( $U=150 \text{ keV}$ , microfocus tube) with a spatial resolution of 22  $\mu\text{m}$ . This was only possible due to the low thickness of the sample because the attenuation of the BiSn sample is significant in this case. The result shown in Fig. 1(c) displays void structures in several positions of the sample corresponding well to the features detected in the neutron dark-field image. However, it becomes obvious in the x-ray image that the voids have sizes of up to 150–500  $\mu\text{m}$  and are hence too big to provide USANS signals. These structures are in the range of the limit of the spatial resolution of the neutron instrument. However, the attenuation contrast is too low to image them, and because the shapes are highly irregular, the differential phase effects they induce are not detected as such. That means that the

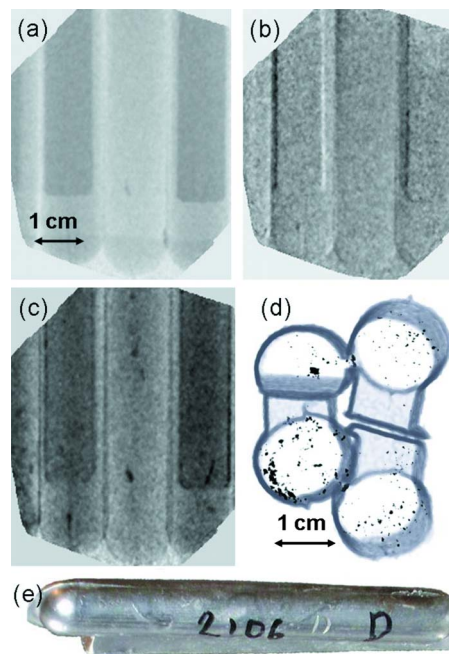


FIG. 2. (Color online) (a) Attenuation, (b) differential phase, and (c) dark-field contrast of cast AlSi ingots containing different amounts of hydrogen in the initial melt (four samples side by side). (d) Volumetric representation of dark-field contrast tomography reconstruction (top view of four samples). (e) A photograph of one sample.

beam is refracted at the structures. However, due to the irregular shapes of the structures, beam deviations to different directions occur within areas of the size of the spatial resolution. Hence, diminished amplitudes of the interference pattern typical for dark-field contrast are found rather than phase shifts, as would be expected for refraction.<sup>16,18,19</sup> Consequently, structures of the order of the spatial resolution can cause dark-field contrast despite of the fact that they are too big to cause significant USANS [Fig. 1(d)].

Another class of samples investigated were cast binary AlSi ingots with approximately cylindrical shapes obtained using Ransley molds. These samples are relevant materials for the aircraft and automotive industry and the effects of different amounts of hydrogen in the liquid metal prior to casting was being evaluated on the internal structure and homogeneity. Corresponding hydrogen contents in the liquid metal ranged from trace amounts of up to 0.36 ml/100 g. The initial radiographic images display inhomogeneities with respect to inner structures in attenuation as well as dark-field contrast in some samples, while the differential phase images provide contrast only due to the edges of the outer shape of the samples [Fig. 2(a)]. However, significantly more types and amount of features are visible in the dark-field images. As the features displayed in the attenuation contrast image are of higher attenuation than the surrounding material, it can be speculated that these might be pores filled with hydrogen (or other inclusions). Therefore it is likely that structures of similar size displayed only in the dark-field image might be hollow pores. The dark-field images show clearly that microscopic structures are present in the samples and these are very different for the samples of different castings. In the radiography, these signals are superposed by contrast differ-

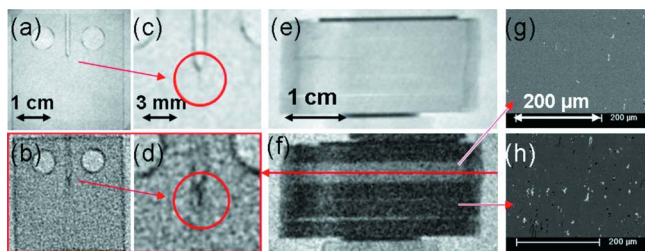


FIG. 3. (Color online) (a) Dark-field contrast radiography (b) and tomography of Al fatigue test sample; (c) and (d) are corresponding details of the images in (a) and (b) highlighting microcracks in the interior of the specimen. (e) and (f) are attenuation and dark-field contrast radiographies of five fatigue test samples in the tomography geometry. The second sample from top corresponds to (a)–(d) as well as to the SEM image in (g). (h) is a SEM image of one of the other samples [4th from top in (e) and (f)].

ences due to different sample thicknesses in the specific area. Therefore, a tomographic scan was performed with these samples. One hundred and one projection images were recorded, respectively, derived from the grating scans in each angular position. The result of a reconstruction of the dark-field signal such as described in Strobl *et al.*<sup>18,19</sup> is given in Fig. 2. The image displays the mentioned structural heterogeneities in three dimensions. A more detailed analyses of the results, together with complementary studies on these samples, is beyond the scope of this paper and will be given elsewhere.

As a third application, radiographic and tomographic measurements were also performed on five Al alloy fatigue test samples. All samples had outer dimensions of  $31 \times 33 \times 2.7$  mm<sup>3</sup>. In the volume of one specific sample microcracks due to fatigue damage could be identified in the radiographic image as well as in the tomographic slices [Figs. 3(a)–3(d)]. All samples were Al-alloys with similar concentrations of Cu (2%–4.3%), Mg (2.3%–2.7%), Mn (0%–0.7%), and Si (0%–0.4%). Consequently, they could not be distinguished in attenuation based images [Fig. 3(e)]. However, one of them is found to display significantly different contrast in the dark-field images [Fig. 3(f)] and is therefore expected to differ correspondingly in its microstructure. In order to verify this finding, the Al specimens were subjected to scanning electron microscopy (SEM) investigations which support the conclusions drawn based on the dark-field contrast images [Figs. 3(g) and 3(h)]. The specimen providing the low dark-field contrast is much more homogeneous in its microstructure and displays significantly less pores and inclusions, both of which give rise to ultras-small-angle scattering for the found size range between 0.5 and around 10 μm. Additionally, energy dispersive x-ray measurements showed that the precipitates in the high contrast samples contain considerably higher concentrations of Cu, which increases the scattering length contrast, as compared to the matrix material, and are hence appropriate to increase the scattering from these structures. Consequently, in the case of these Al samples, not only a structural defect due to a fatigue loading, but also microstructural differences, which are most likely related to the sample manufacture and treatment, and which

are not amenable to conventional neutron imaging techniques could be resolved and visualized.

Measurements on various samples with a grating interferometer for neutron imaging have demonstrated that microscopic structures and inhomogeneities on a size range from below 1 μm to several hundreds of micrometers, i.e., about two orders of magnitude but beyond the real space spatial resolution of the imaging setup could be identified and located three-dimensionally. The information content of dark-field contrast investigations could be shown to be complementary to that achieved with more conventional techniques such as attenuation and phase contrast. However, different origins of the dark-field signal have to be taken into account, namely, ultras-small-angle scattering and refraction, which might complicate a straightforward interpretation of specific results with respect to the quantification of the size of inhomogeneities and defects. The application of the method in different investigations and the promising results also in comparison to attenuation and differential phase contrast clearly underline the outstanding potential of the novel method for various material science and engineering applications.

<sup>1</sup>M. Strobl, I. Manke, N. Kardjilov, A. Hilger, M. Dawson, and J. Banhart, *J. Phys. D* **42**, 243001 (2009).

<sup>2</sup>E. Lehmann, G. Frei, G. Kühne, and P. Boillat, *Nucl. Instrum. Methods Phys. Res. A* **576**, 389 (2007).

<sup>3</sup>A. S. Tremsin, J. V. Vallerga, J. B. McPhate, O. H. W. Siegmund, W. B. Feller, L. Crow, and R. G. Cooper, *Nucl. Instrum. Methods Phys. Res. A* **592**, 374 (2008).

<sup>4</sup>M. Strobl, N. Kardjilov, A. Hilger, G. Kühne, G. Frei, and I. Manke, *Nucl. Instrum. Methods Phys. Res. A* **604**, 640 (2009).

<sup>5</sup>B. Schillinger, J. Brunner, and E. Calzada, *Physica B* **385–386**, 921 (2006).

<sup>6</sup>A. Hillenbach, M. Engelhardt, H. Abele, and R. Gähler, *Nucl. Instrum. Methods Phys. Res. A* **542**, 116 (2005).

<sup>7</sup>N. Kardjilov, A. Hilger, I. Manke, M. Strobl, W. Treimer, and J. Banhart, *Nucl. Instrum. Methods Phys. Res. A* **542**, 16 (2005).

<sup>8</sup>N. Kardjilov, I. Manke, M. Strobl, A. Hilger, W. Treimer, M. Meissner, T. Krist, and J. Banhart, *Nat. Phys.* **4**, 399 (2008).

<sup>9</sup>M. Dawson, I. Manke, N. Kardjilov, A. Hilger, M. Strobl, and J. Banhart, *New J. Phys.* **11**, 043013 (2009).

<sup>10</sup>J. R. Santisteban, L. Edwards, A. Steuwer, and P. J. Withers, *J. Appl. Crystallogr.* **34**, 289 (2001).

<sup>11</sup>W. Kockelmann, G. Frei, E. H. Lehmann, P. Vontobel, and J. R. Santisteban, *Nucl. Instrum. Methods Phys. Res. A* **578**, 421 (2007).

<sup>12</sup>W. Treimer, M. Strobl, N. Kardjilov, A. Hilger, and I. Manke, *Appl. Phys. Lett.* **89**, 203504 (2006).

<sup>13</sup>B. E. Allman, P. J. McMahon, K. A. Nugent, D. Paganin, D. L. Jacobson, M. Arif, and S. A. Werner, *Nature (London)* **408**, 158 (2000).

<sup>14</sup>N. Kardjilov, E. Lehmann, E. Steichele, and P. Vontobel, *Nucl. Instrum. Methods Phys. Res. A* **527**, 519 (2004).

<sup>15</sup>M. Strobl, W. Treimer, and A. Hilger, *Nucl. Instrum. Methods Phys. Res. B* **222**, 653 (2004).

<sup>16</sup>F. Pfeiffer, C. Grünzweig, O. Bunk, G. Frei, E. Lehmann, and C. David, *Phys. Rev. Lett.* **96**, 215505 (2006).

<sup>17</sup>M. Strobl, W. Treimer, and A. Hilger, *Appl. Phys. Lett.* **85**, 488 (2004).

<sup>18</sup>M. Strobl, C. Grünzweig, A. Hilger, I. Manke, N. Kardjilov, C. David, and F. Pfeiffer, *Phys. Rev. Lett.* **101**, 123902 (2008).

<sup>19</sup>M. Strobl, A. Hilger, N. Kardjilov, O. Ebrahimi, S. Keil, and I. Manke, *Nucl. Instrum. Methods Phys. Res. A* **605**, 9 (2009).

<sup>20</sup>A. Hilger, N. Kardjilov, M. Strobl, W. Treimer, and J. Banhart, *Physica B* **385–386**, 1213 (2006).